University of Bath

Alternative formats
If you require this document in an alternative format, please contact:
openaccess@bath.ac.uk

1   **Title:** Macropore structure and permeability of clay fill samples from a historic clay fill earthwork

2

3   **Authors:** D. M. Muddle[1] & K.M. Briggs[1]*

4   [1]Department of Architecture & Civil Engineering, University of Bath, Bath, UK. BA2 7AY.

5   *Corresponding author

6

7   **Words:** 4391 (main text)

8   **Tables:** 6

9   **Figures:** 13

10

11   **Abstract:**

12   Near surface macropores and macro features (e.g. cracks and fissures) provide pathways for rapid
13   water infiltration into the core of clay fill earthworks. However it is more difficult to measure the size
14   and distribution of macropores located below the weathered soil surface (>1.5 m depth) and hence
15   assess their influence on water flow through the clay fill core of an earthwork.

16   This paper explores the influence of macropores on the rate of water flow within the core of a
17   historic railway earthwork. Samples were excavated from the core (1.5 m – 6.5 m depth) of a clay fill
18   railway embankment and subjected to laboratory saturated hydraulic conductivity testing. The
19   samples were scanned using X -ray computed tomography (XCT) before and after laboratory testing.
20   XCT was used to measure the size and distribution of macropores (>63 ×10^{-6} m) within the samples
21   and compare with the saturated hydraulic conductivity measurements.

22   The results showed that the distribution of macropores and the saturated hydraulic conductivity of
23   the samples from the embankment core was not dependant on the depth of excavation. The total
24   macroporosity of the samples was very small relative to the total porosity (less than 10%). The
25   saturated hydraulic conductivity of the samples was more closely related to the connectivity of the
26   macropores (mean length) than to the total porosity or the total macroporosity.

27   The macropores were variably distributed within the core of the clay fill embankment, they did not
28   show a clear relationship with depth and they were connected over relatively short lengths (the
29   mean macropore length was not greater than 1.6 ×10^{-3} m). Therefore water flow through the core of
30   the embankment is likely to be through the clay fill matrix, rather than through the connected
31   macropore pathways which allow rapid water infiltration at the near soil surface (<1.5 m depth).

1. Introduction

Changes in pore water pressure critically influence the strength and volume change of clay fill soils. This affects the long-term performance (deformation and stability) of earthworks constructed from these materials (Glendinning *et al.*, 2014; Briggs *et al.*, 2017). Such structures include new and historic railway and highway embankments, flood embankments and embankment dams.

There is evidence that near surface macropores and macro features (e.g. cracks and fissures) provide pathways for rapid water infiltration into the core of clay fill earthworks (Dyer *et al*, 2009; Li *et al.*, 2011; Dixon *et al.*, 2018). This can increase the rate of pore water pressure rise within earthworks in response to environmental changes such as precipitation and flooding events. Macropores can also act as preferential flow paths in soils below the near surface zone (Beven & Germann, 2013). However, there is limited data showing the size and connectivity of macropores within the core of clay fill embankments. Therefore, it is difficult to establish whether preferential flow occurs through connected macropores or through the clay fill matrix; as is assumed in simulations of embankment hydrology (Kovacevic *et al.*, 2001; Scott *et al.*, 2007; O'Brien, 2013, Briggs *et al.*, 2016).

It can be difficult to measure the size and distribution of macropores within soils without disturbing the sample structure. Recent research (e.g. Perret *et al.*, 1999; Mooney, 2002; Mees and London, 2003; Luo *et al.*, 2008; Anderson *et al.*, 2010; Peth *et al.*, 2010; Mooney *et al.*, 2012; Geistlinger, 2013; Naveed *et al.*, 2013; Shin *et al.*, 2013; Lamorski *et al.*, 2014; Larsbo *et al.*, 2014; Katuwal *et al.*, 2015; Eck *et al.*, 2016) has explored the use of computed tomography to visualise macropore structure within small (<50 mm) samples of reconstituted soil. However, the technique has not been used to measure macropores within larger, denser samples of *in situ* clay fill, nor has it been used to explore the distribution of macropores through the core of an earthwork.

This paper presents an investigation into the use of X-ray computed tomography (XCT) to visualise and measure macropore structure ($>63 \times 10^{-6}$ m) within 100 mm diameter samples of clay fill. XCT and laboratory testing is used to explore relationships between the macropore structure and saturated hydraulic conductivity of clay fill samples obtained from the core (1.5 m to 6.5 m depth) of a historic railway earthwork.

2. Method

Soil samples were obtained from Laverton Embankment (Figure 1) in Gloucestershire, in south-west England. The embankment is approximately 6m high and it was built between 1900 and 1906 as part of the Honeybourne Line, which now forms the Gloucestershire-Warwickshire Steam Railway. Many railway embankments of this period were constructed by end-tipping locally excavated clay to form poorly compacted, 'dumped' clay fill embankments (Vaughan *et al.*, 2004; Briggs *et al.*, 2017).

Six soil cores (87-102 mm diameter, 160 mm height) were extracted from a borehole at the crest of Laverton Embankment at approximately 1m intervals between 1.5 m and 6.5 m depth. Intact samples were obtained from within the core of the earthwork rather than from the more variable near surface soil (<1.5 m depth), where dynamic weathering processes (e.g. desiccation cracking, plant roots) and seasonal soil moisture variation would influence the soil structure (Smethurst *et al.*, 2003; Glendinning *et al.*, 2014; Dixon *et al.*, 2018). Boreholes drilled along the length of the embankment showed that a variable upper layer of fouled ballast (approximately 0.9 m thick) overlaid clay fill formed from locally excavated, end-tipped Charmouth Mudstone (Gunn *et al.*, 2016). The cores were collected using cable-percussion drilling with a Dando Terrier 2002 rig. This allowed the recovery of continuous 1 m long samples captured in polyvinyl chloride (PVC) liners. The diameter of the two deepest cores was reduced from 102 mm to 87 mm during drilling to reduce

76 sampling resistance at these depths. The sample from 6.5 m depth was disturbed during drilling so it
77 was not possible to determine if this was clay fill or clay from the embankment foundation.

78 While it is difficult to obtain perfectly undisturbed samples for testing (Clayton and Siddique, 2001),
79 disturbance was minimalised in every part of the sampling process. After trimming, the samples
80 were stored in PVC tubes with secure end caps to prevent mechanical disturbance and evaporation.
81 The samples were stored in a refrigerator at 3°C. Table 1 shows the size, sampling depth, bulk
82 density and gravimetric water content of the samples. A 100 mm diameter, reconstituted sample
83 was prepared from sample 4C (3.5 m depth) using wet compaction to a bulk density of 1.91×10^{-3}
84 kg/m^3. Particle size distributions were obtained for the samples from 3.5 m and 4.5 m depth using
85 wet sieving and hydrometer tests (BS 1377-2:1990). These showed that the samples were well
86 graded, consisting of 45% clay, 50% silt and 10% sand particles. Soil index testing showed that the
87 liquid and plastic limits of the samples were between 61-77% and 27-37% respectively. X-Ray
88 diffraction analysis of the clay fill was undertaken using a Bruker D8 Advance X-ray powder
89 diffractometer with CuKa radiation. This showed that the clay fraction of the fill ($<2 \times 10^{-6}$ m)
90 consisted of Quartz, Calcite, Kaolinite, Illite and Sodium Magnesium Aluminium Silicate.

91 XCT scans were undertaken at multiple stages in the laboratory testing process. First, the samples
92 were scanned to obtain macropore information prior to laboratory testing. Second, the samples
93 were saturated within a triaxial cell and subjected to constant head permeability testing. The
94 samples were then removed and scanned in the saturated condition. Finally, the triaxial cell samples
95 were divided into three smaller samples and subjected to one-dimensional consolidation tests. The
96 details relating to each of these stages is described in more detail below.

2.1 XCT scanning and analysis procedure

98 X-ray computed tomography is a 3D imaging process that is based on the principle of
99 electromagnetic wave attenuation. X-rays emitted from the source pass through the sample and are
100 attenuated by absorption and scattering (Mooney et al., 2012). The degree of attenuation along any
101 x-ray path is controlled by the materials it passes through (each of which has a linear attenuation
102 coefficient (μ) dependent on the electron density of the material) and the X-ray energy. The X-rays
103 are then converted to photons and recorded using a scintillator-fronted detector. As the sample is
104 rotated, 2D grey-scale images (projections) are collected from many angles. Each image records the
105 total attenuation of the X-rays. The 2D projection data are then reconstructed into a 3D volume
106 using numerical algorithms, and can then be visualised as a 3D voxelised volume (a voxel is the 3D
107 equivalent of a pixel) where the intensity or brightness of each voxel represents the attenuation, and
108 therefore density of the material in that voxel volume. The size of the voxels reflects the spatial
109 resolution of the scan.

110 Although visual inspection is a valuable qualitative tool, the image data can be quantified using
111 software packages such as Avizo (FEI Visualization Sciences Group), CT Analyser (Skyscan-Bruker) or
112 Fiji (Schindelin et al., 2012). As the greyscale is related to the material composition, the porosity of a
113 material, or the volume fraction of any phase (e.g. solid, liquid) or mineral can be determined by
114 counting the number of voxels assigned to it during segmentation of the sample (see Appendix).
115 Quantitative 3D analysis is made challenging by artefacts within the image data (e.g. image noise,
116 beam hardening, ring artefacts), poor greyscale contrast between the different phases and minerals
117 (better contrast is achieved at lower energies but at the cost of poorer transmission and lower signal
118 to noise), and insufficient spatial resolution (often called the partial voxel effect) which causes a
119 voxel to be made up of several minerals or phases and causes averaging and blurring of phase
120 boundaries (Cnudde & Boone, 2013). For these reasons, CT investigations in the geosciences (Pender

121 *et al.*, 2009; Ito & Azam, 2017; Wildenschild & Sheppard, 2013) have generally used smaller sample
122 sizes (< 50 mm).

123 The samples were scanned using a Nikon X-Trek XTH225ST with a maximum accelerating voltage of
124 195kV at 105 mA. The beam was pre-filtered using 0.5 mm Cu to reduce beam hardening. A total of
125 1800 projections were taken over 360-degree rotation with a two-second exposure time. Data were
126 reconstructed using the Nikon proprietary filtered back projection algorithm, with a voxel resolution
127 of 53-63 $\times 10^{-6}$m (see Table 3; after Muddle, 2017).

128 The XCT scan settings shown in Table 2 were used to examine the clay fill samples. Initial
129 investigations (Muddle, 2017) showed that it was not possible to scan a larger (300 mm) block
130 sample of clay fill without reducing image resolution, losing greyscale contrast between the mineral
131 phases and forming excessive imaging artefacts such as beam hardening.

132 The image processing and interpretation followed the procedure developed by Muddle (2017), as
133 outlined in the Appendix. The images were reconstructed using the Nikon proprietary software
134 (Nikon, 2019). The software contains correction algorithms to reduce ring artefacts, beam hardening
135 and noise. The same reconstruction settings were used for each sample to aid comparison of the
136 data and the repeatability of the tests. However the impact of these algorithms on the image
137 reconstruction were not explored, hence they may not represent the best available method.

138 Four different methods of image enhancement were explored (a median filter, sharpened filter, non-
139 local means filter and Gaussian filter). The effectiveness of these methods was measured by
140 comparing the degree of contrast from the image slices and greyscale histograms. A sharpened
141 median filter was identified as the most effective and computationally efficient image improvement
142 process (see Appendix). Initial investigations showed that automated watershed thresholding
143 (Iassonov et al., 2009), was not appropriate for the clay fill samples (see Appendix). Manual
144 interactive thresholding was required for the clay fill samples because they were dense samples with
145 intensity histograms that lacked complete definition. A two-voxel partial volume correction was used
146 for the clay fill samples because it minimally altered the macroporosity measurement (less than
147 0.04% for the samples tested) but removed a large number of objects from the image. The influence
148 of the partial volume correction on the measured pore properties is shown in the Appendix.

149 Preliminary investigations (Muddle, 2017) were used to develop a rigorous and repeatable image
150 analysis method, which allowed the macropore properties of the clay fill samples shown in Table 1
151 to be compared. Due to the inherent variability of the 100 mm diameter samples, the scans were
152 performed at a range of voxel sizes. Table 3 shows the voxel resolution achieved from each scan. To
153 keep the resolution constant between repeated scans of the same sample and to allow for
154 comparison of the evolution of the macropore structure with saturation, the partial volume effect
155 correction was matched between corresponding samples. A 40 mm sub volume at the centre of the
156 sample was used for subsequent image processing and analysis, to reduce computational demand.

157 The consistency of the image analysis procedure was explored by examining the results of the three
158 scans over the height of sample 5C (at the top, middle, and bottom of the sample). Data from three
159 individual scans was processed independently; however there was some crossover (overlap) in the
160 scans. This allowed the scans to be compared, showing that the volume of voids per slice in the
161 sample aligned almost exactly (Figure 2).

162 ## 2.2 Saturated hydraulic conductivity testing
163 Saturated hydraulic conductivity (K_{sat}) measurements were undertaken using the samples from
164 Laverton Embankment. This allowed a direct comparison with the macropore property metrics

165 measured using XCT. However it should be noted that this sample size (102 mm diameter) may limit
166 the ability to measure the permeable fabric within a clay fill embankment, which requires 250 mm
167 diameter samples (Rowe, 1972), or *in situ* testing to measure the presence of larger cracks and
168 fissures within the near surface (<1.5 m depth) soil (Dixon *et al.*, 2018).

169 The samples were installed in the triaxial cell and saturated using backpressure saturation (B-ratio >
170 95%). The use of CO_2 flushing was explored to achieve higher saturation, but this was ineffective.
171 The effective stresses applied to the samples replicated field conditions at the depth from which the
172 samples originated (Table 1). Constant head permeability tests were undertaken according to BS
173 1377-5:1990 (British Standards Institution, 1990) using a hydraulic gradient (*i*) of 125. The
174 saturated hydraulic conductivity was calculated using Darcy's Law (Darcy, 1856).

175 The triaxial samples were divided into three layers and subjected to three, one-dimensional
176 oedometer consolidation tests according to BS 1377-5:1990. The saturated hydraulic conductivity of
177 the samples was calculated using Terzaghi's (1943) consolidation theory.

2.3 Mercury intrusion porosimetry (MiP) testing

179 Mercury intrusion porosimetry (MiP) testing was undertaken using the reconstituted sample and
180 sample $5C_{(bot)}$ from 4.58 m depth. This was used to measure pores in the samples which were not
181 captured by the XCT technique. MiP involves applying an absolute pressure to mercury (a non-
182 wetting fluid) in order to force it to enter pores within the sample. If the pores are assumed to be of
183 cylindrical shape then the pore diameter can be estimated using the Washburn equation (Washburn,
184 1921). The surface tension of mercury was taken to be equal to 0.484 N/m at 25°C (Smith, 2015).
185 The contact angle between mercury and the pore wall is usually taken between 139° and 147° for
186 clays (Diamond, 1970), so 140° was used in these tests.

187 Mercury intrusion porosimetry can be used to estimate porosity for pore diameters between 4×10^{-9}
188 m and 0.4×10^{-3} m. This is a much finer resolution than is possible using XCT (greater than 50×10^{-6}
189 m). However, MiP does have several limitations when applied to this investigation. First, it is not
190 possible to measure isolated pores that are completely enclosed by solids and it is not possible to
191 measure pores that are only accessible through smaller ones. Second, the minimum practical
192 pressure of the machine limits the largest size of pore that can be measured. Mostly critically, MiP
193 requires the use of very small samples (less than 0.001kg) which must be oven dried or freeze-dried
194 prior to testing. This limits the usefulness of MiP when investigating the influence of macropores on
195 the saturated hydraulic conductivity of the clay fill samples (i.e. the pores with a diameter $>0.4 \times 10^{-3}$
196 m). However, it does give an indication of the volume of pores that were not captured by the XCT
197 images, as a useful comparison. Oven drying of the samples and phase relationships (Powrie, 2014)
198 were used to obtain the total porosity of the samples over the full range of pore diameter sizes.

2.4 Method to compare the strength of association between the XCT results and the results of conventional laboratory testing

201 The correlation between the XCT derived property metrics and the laboratory measurements of
202 sample porosity (*n*), density (*ρ*), and saturated hydraulic conductivity (K_{sat}), were examined using
203 Spearman's (1904) correlation coefficient (r_s);
204

$$r_s = 1 - \frac{6\sum D^2}{N^3 - N}$$

206

207 Where, *D* is the difference between the two ranks of each observation and *N* is the number of
208 observations. Spearman's correlation coefficient is a non-parametric test used to measure the
209 strength of association between two variables, where r_s = 1 means a perfect positive correlation and
210 the r_s = -1 means a perfect negative correlation.

3. Results

212 The total macroporosity within the samples (after Partial Volume Effect correction, see Table 4)
213 ranged from 0.12 % to 4.12 % and the mean macropore length varied between 0.80 ×10^{-3} m and 1.6
214 ×10^{-3} m (excluding sample 7C). These values are similar in magnitude to those derived from CT scans
215 of soils reported in the literature (Luo *et al*., 2010 (silt loam samples); Naveed *et al*., 2013 (clay and
216 sandy clay samples); Shin *et al*., 2013 (artificial clay samples); Larsbo *et al*., 2014 (clay loam
217 samples)).

218 The macropore structure within each of the samples (2C to 7C) was variable (Figure 3). Some
219 samples contained large, isolated macropores (Figure 3a), some contained biological-type pores
220 running through the sub volume (Figure 3b) and the reconstituted sample (Figure 3c) contained a
221 more uniform size and spatial distribution of macropores. A comparison of the volume of voids per
222 slice in each of the samples shows that there is no clear variation in the distribution of macropores
223 with depth within the embankment core (Figure 4). This was also evident in the three dimensional
224 macropore visualisations (e.g. as shown in Figure 3). These visualisations showed that Sample 7C was
225 heavily fractured because of disturbance during excavation. This is evidenced by the large range of
226 the volume of voids in Sample 7C (Figure 4).

227 The laboratory saturation procedure reduced the total macroporosity, the macropore density and
228 the macropore surface area density within the samples (Table 4). Some consolidation may have
229 occurred due to the high hydraulic gradient used for the test, or when the pore pressure within the
230 samples was lowered (relative to the cell pressure) before they were removed from the triaxial cell
231 (Pender *et al*., 2009). Figure 5 shows the pore size distribution per slice (as a percentage of total
232 pore volume) through the 40 mm cubed sub volumes in samples 2C, 3C and 4C. This shows that the
233 saturation procedure decreased the volume of pores per slice and increased the macropore
234 uniformity of the samples. The saturation procedure also reduced the size of the largest macropores
235 within each sample, indicating that these pores are more likely to be affected by the saturation
236 procedure than the smaller pores within the samples. This is in agreement with evidence showing
237 that larger pores close first during the compaction of sediments (Delage & Lefebvre, 1984).

238 The results of the MiP tests for Sample 5C$_{(bot)}$ and the Reconstituted Sample are shown in Table 5.
239 The porosity measured using the MiP technique was significantly lower than that measured using
240 phase relationships (e.g. 26% and 50% respectively for the Reconstituted Sample). The MiP data
241 showed that the samples contained a modal pore diameter of 0.05 ×10^{-6} m. This is one thousand
242 times smaller than can be observed using the XCT images. Both the MiP and the total porosity values
243 are much larger than the porosity of the samples measured using XCT. This shows that the most
244 significant proportion of the total porosity consists of pores that are smaller than the macropores
245 (>63 ×10^{-6} m). However, the fewer, larger pores may still influence water flow. Experimental
246 evidence suggests that pores larger than 0.3 ×10^{-3} m in equivalent cylindrical diameter are the main
247 pathways for rapid, non-equilibrium flow (Jarvis, 2007). This indicates that the XCT pore property
248 metrics will be more representative of these larger pores than the pore sizes measured using total
249 porosity or MiP.

250 The saturated hydraulic conductivity (K_{sat}) measurements from triaxial permeability tests and one-
251 dimensional consolidation tests are compared in Table 6. The K_{sat} measured using the triaxial
252 samples was consistently lower than that measured using the oedometer samples. The values of K_{sat}
253 are comparable with laboratory measurements of London Clay fill reported by O'Brien, *et al*. (2004),
254 which showed a median K_{sat} of 8×10^{-10} ms^{-1} (range 3×10^{-9} to 2×10^{-11} ms^{-1}) from 34 laboratory tests.
255 Both the laboratory K_{sat} values shown in Table 6 and those reported by O'Brien *et al*. (2004) are
256 approximately two orders of magnitude lower than those measured for clay fill using *in situ* testing
257 methods (O'Brien *et al*., 2004; Dixon *et al*., 2018).

258 Figure 6 shows the Spearman's correlation coefficients for the XCT derived macropore property
259 metrics and the laboratory measurements of sample porosity, density and saturated hydraulic
260 conductivity (at the triaxial scale and the oedometer scale). This shows that the total (phase
261 relationship) porosity has a negative correlation to both the triaxial and the oedometer
262 measurements of saturated hydraulic conductivity. There is a mild ($r_s = 0.39$) correlation between
263 the triaxial K_{sat} and the total macroporosity derived from the XCT data. A closer ($r_s = 0.71$) correlation
264 is shown between the total macroporosity and the oedometer K_{sat}. The XCT measured mean
265 macropore length shows a strong positive correlation with the K_{sat} measured using both the triaxial
266 cell ($r_s = 0.96$) and the oedometer ($r_s = 0.86$). This shows that the saturated hydraulic conductivity of
267 the samples was influenced by the length of the macropores, rather than the quantity of macropores
268 (total macroporosity).

269 Reference to Table 4 and Table 6 shows that the samples with the greatest mean macropore length
270 had the highest saturated hydraulic conductivity. The mean macropore length represents a measure
271 of the connectivity of macropores within the samples. This shows that the connected macropores
272 were small (mean macropore length up to 1.6×10^{-3} m) but sufficient to provide preferential flow
273 pathways through the samples. Experimental evidence (Jarvis, 2007) and conceptual models (Jarvis
274 *et al*., 2016; Jang *et al*., 2011) show that this occurs in soils which contain large continuous
275 macropores but lack well-connected networks of smaller macropores.

276 There is a closer correlation between the pore property metrics and the oedometer K_{sat}
277 measurements than with the triaxial K_{sat} measurements. Figure 6 shows a close correlation between
278 the K_{sat} measured using the oedometer and all of the pore property metrics. This is because the XCT
279 sub volumes (40 mm cubes) are more representative of the scale and hence the macropore
280 distribution of the oedometer samples (20 mm thick) than the triaxial samples (80 mm thick).
281 Munkholm *et al.* (2012) showed similar results for scans of agricultural soils, in that the strongest
282 correlations were found between parameters assessed at similar levels of observation. Visual
283 inspection of the samples (e.g. Figure 3) showed that the macropores extended through lengths
284 equivalent to the oedometer samples but not throughout the full height of the triaxial samples.

4. Conclusions

286 XCT was used to visualise and quantify the pore structure within 100 mm diameter clay fill samples
287 at a resolution that enabled the measurement of macropores ($> 63 \times 10^{-6}$ m). The samples were
288 scanned in both partially saturated and fully saturated conditions to investigate the evolution of the
289 internal macropore structure following saturation. Additionally, XCT-derived pore property metrics
290 were compared to saturated hydraulic conductivity measurements to assess the influence of
291 macroporosity on water flow. The following conclusions can be drawn:

292 1) The XCT results show that the distribution of macropores ($>63 \times 10^{-6}$ m) was variable throughout
293 the embankment core (between 1.5 m and 6.5 m depth). The saturated hydraulic conductivity (K_{sat})

294 of the samples also varied throughout the embankment core, showing no clear relationship with
295 depth. Comparative macropore data from other clay fill embankments is not available, but this result
296 is representative of the variable, poorly compacted nature of the dumped clay fill (Vaughan *et al*.,
297 2004; Briggs *et al*., 2017). This is in contrast to the relationship of decreasing K_{sat} with depth
298 measured in overconsolidated clay cuttings (Chandler, 1974; Dixon *et al*., 2018).

299 2) The macropore length had a greater influence on the saturated hydraulic conductivity (K_{sat}) than
300 the total porosity within the laboratory-scale samples. This relationship was more evident for the
301 oedometer samples with a short (20 ×10^{-3} m) flow path than for the triaxial samples with a longer
302 (80 ×10^{-3} m) flow path. The macropores increased the permeability of the samples, but they were
303 connected over relatively short lengths (the mean macropore length was up to 1.6 ×10^{-3} m).
304 Therefore the assumption of matrix-dominated flow used in simulations of embankment hydrology
305 (Kovacevic *et al*., 2001; Scott *et al*., 2007; O'Brien, 2013, Briggs *et al*., 2016) is likely to be
306 representative of the clay fill in the embankment core at Laverton. However, it may not be
307 representative of embankments formed with lenses of alternative materials (e.g. a widened or
308 repaired embankment), or representative of clay fill soil near the surface (<1.5 m depth), where
309 visible cracks and fissures can develop over greater lengths (Dixon *et al*., 2018).

310 3) The process of saturation and laboratory testing altered the macropore structure of the clay fill
311 samples. The largest macropores within the samples were most affected by the saturation
312 procedure and were more sensitive to disturbance and small stress changes than the smaller pores.
313 This is in agreement with measurements taken during the compaction of sediments (Delage &
314 Lefebvre, 1984) and the consolidation of residual clay (Pender *et al*., 2009). Therefore the
315 contribution of macropores to water flow within clay fill soils at low effective stress (e.g. within in a
316 small embankment) may not be captured during laboratory testing; leading to underestimates of the
317 *in situ* water flow and storage characteristics (e.g. permeability, porosity).

5. Acknowledgements

324

6. References

Ambrose, J. (1973) Computerized Transverse Axial Scanning (Tomography): Part 2: Clinical Application', *British Journal of Radiology*, 46, p. 1023

Anderson, S.H., Udawatta, R.P., Kumar, S., Gantzer, C.J., Rachman, A., Gilkes, R.J., Gilkes, R. and Prakougkep, N. (2010). CT-measured macropore parameters for estimating saturated hydraulic conductivity at four study sites. In *19th World Congress of Soil Science, Soil Solutions for a Changing World, Brisbane, Australia*,pp. 13-16.

Beven, K. and Germann, P. (2013) Macropores and water flow in soils revisited, *Water Resources Research*, 49(6), pp. 3071–3092. doi: 10.1002/wrcr.20156.

Briggs, K.M, Smethurst, J.A., Powrie, W. and O'Brien, A.S. (2016). The influence of tree root water uptake on the long term hydrology of a clay fill railway embankment. *Transportation Geotechnics,* 9, 31–48.

Briggs, K.M., Loveridge, F. A. and Glendinning, S. (2017) Failures in transport infrastructure embankments, *Engineering Geology*. Elsevier B.V., 219, pp. 107–117. doi: 10.1016/j.enggeo.2016.07.016.

British Standards Institution (1990). 1377–2: *Methods of test for soils for civil engineering purposes—Part 2: classification tests*.

British Standards Institution (1990). 1377–5: *Methods of test for soils for civil engineering purposes—Part 5: Compressibility, permeability and durability tests.*

Chandler, R.J. (1974). Lias clay: the long-term stability of cutting slopes. *Géotechnique*, 24(1), pp.21-38.

Clayton, C.R.I. and Siddique, A. (1999). Tube sampling disturbance—forgotten truths and new perspectives. *Proceedings of the Institution of Civil Engineers-Geotechnical Engineering*, *137*(3), pp.127-135.

Clothier, B.E., Green, S.R. and Deurer, M. (2008). Preferential flow and transport in soil: progress and prognosis. *European Journal of Soil Science*, 59(1), pp.2-13.

Cnudde, V. and Boone, M.N. (2013) High-resolution X-ray computed tomography in geosciences: A review of the current technology and applications, *Earth-Science Reviews*. Elsevier B.V., 123, pp. 1–17. doi: 10.1016/j.earscirev.2013.04.003.

Darcy, H. (1856). *Les fontaines publiques de la ville de Dijon*Dalmont, Paris.

Delage, P. and Lefebvre, G. (1984). Study of the structure of a sensitive Champlain clay and of its evolution during consolidation. *Canadian Geotechnical Journal*, 21(1), pp.21-35.

Diamond, S. (1970) Pore Size Distributions in Clays, *Clays and Clay Minerals*, 18(1), pp. 7–23. doi: 10.1346/CCMN.1970.0180103.

Dixon, N., Crosby, C.J., Stirling, R., Hughes, P.N., Smethurst, J., Briggs, K., Hughes, D., Gunn, D., Hobbs, P., Loveridge, F.A., Glendinning, S., Dijkstra, T. and Hudson, A. (2018). In situ measurements of near-surface hydraulic conductivity in engineered clay slopes. *Quarterly Journal of Engineering Geology and Hydrogeology*.

363   Dyer, M., Utili, S. and Zielinski, M. (2009). Field survey of desiccation fissuring of flood
364   embankments. In *Proceedings of the Institution of Civil Engineers-Water Management*,Vol. 162, No.
365   3, pp. 221-232. Thomas Telford Ltd.

366   Eck, D.V., Qin, M., Hirmas, D.R., Giménez, D. and Brunsell, N.A. (2016). Relating quantitative soil
367   structure metrics to saturated hydraulic conductivity. *Vadose Zone Journal*, *15*(1).

368   Geistlinger, H. (2013) Mass transfer processes across the Capillary Fringe: Quantification of gas-
369   water interface and bubble mediated mass transfer, *EGU General Assembly*, Vienna 15(i), p. 3343

370   Glendinning, S., Hughes, P., Helm, P., Chambers, J., Mendes, J., Gunn, D., Wilkinson, P. and
371   Uhlemann, S. (2014). Construction, management and maintenance of embankments used for road
372   and rail infrastructure: implications of weather induced pore water pressures. *Acta Geotechnica*,
373   *9*(5), pp.799-816.

374   Gunn, D., Dashwood, B.A., Bergamo, P. and Donohue, S. (2016). Aged embankment imaging and
375   assessment using surface waves. *Proceedings of the Institution of Civil Engineers-Forensic
376   Engineering*, *169*(4), pp.149-165.

377   Hounsfield, G. (1973) Computerized transverse axial scanning (tomography): part 1. Description of
378   system, *British Journal of Radiology*, 46, pp. 1016–1022.

379   Iassonov, P., Gebrenegus, T. and Tuller, M. (2009). Segmentation of X-ray computed tomography
380   images of porous materials: A crucial step for characterization and quantitative analysis of pore
381   structures. *Water Resources Research*, 45(9).

382   Ito, M. and Azam, S. (2017). Determination of water flow through clayey slurries using computed
383   micro-tomography. *Quarterly Journal of Engineering Geology and Hydrogeology*, *51*(1), pp.49-62.

384   Jang, J., Narsilio, G.A. and Santamarina, J.C. (2011) Hydraulic conductivity in spatially varying
385   media—a pore-scale investigation, *Geophysical Journal International*, Volume 184, Issue 3, 1 March
386   2011, Pages 1167–1179, https://doi.org/10.1111/j.1365-246X.2010.04893.x

387   Jarvis, N.J. (2007). A review of non-equilibrium water flow and solute transport in soil macropores:
388   Principles, controlling factors and consequences for water quality. *European Journal of Soil Science*,
389   58(3), pp.523-546.

390   Jarvis, N., Koestel, J. and Larsbo, M. (2016). Understanding preferential flow in the vadose zone:
391   Recent advances and future prospects. *Vadose Zone Journal*, 15(12).

392   Katuwal, S., Moldrup, P., Lamandé, M., Tuller, M. and De Jonge, L.W. (2015). Effects of CT number
393   derived matrix density on preferential flow and transport in a macroporous agricultural soil. *Vadose
394   Zone Journal*, 14(7).

395   Kovacevic, N., Potts, D.M. and Vaughan, P.R. (2001). Progressive Failure in Clay Embankments Due to
396   Seasonal Climate Changes. *Proceedings of the International Conference on Soil Mechanics and
397   Geotechnical Engineering* Vol. 3. AA Balkema Publishers, pp. 2127–2130.

398   Lamorski, K., Slawinski, C. and Barna, G. (2014) Estimation of water saturated permeability of soils,
399   using 3D soil tomographic images and pore-level transport phenomena modelling, *EGU General
400   Assembly 2014, Vienna, Austria,* (Vol. 16), p. 11775

401 Larsbo, M., Koestel, J. and Jarvis, N. (2014) Relations between macropore network characteristics
402 and the degree of preferential solute transport, *Hydrology and Earth System Sciences*, 18(12), pp.
403 5255–5269. doi: 10.5194/hess-18-5255-2014.

404 Li L.J.H., Zhang L and Kwong B.C.P. (2011) Field permeability at shallow depth in a compacted fill.
405 *Proceedings of the Institution of Civil Engineers – Geotechnical Engineering* 164(3): 211–221.

406 Luo, L., Lin, H. and Halleck, P. (2008) Quantifying Soil Structure and Preferential Flow in Intact Soil
407 Using X-ray Computed Tomography, *Soil Science Society of America Journal,* 72(4), pp. 1058–1069

408 Luo, L., Lin, H. and Li, S. (2010) Quantification of 3-D soil macropore networks in different soil types
409 and land uses using computed tomography, *Journal of Hydrology*. Elsevier B.V., 393(1–2), pp. 53–64.
410 doi: 10.1016/j.jhydrol.2010.03.031.

411 Mees, F., Swennen, R., Van Geet, M. and Jacobs, P. (2003). Applications of X-ray computed
412 tomography in the geosciences. *Geological Society, London, Special Publications*, 215(1), pp.1-6.
413 Nikon (2019). *Insight into the inside. Industrial X-ray and CT.* Nikon Metrology Europe NV. Belgium.

414 Mooney, S. (2002) Three-dimensional visualization and quantification of soil macroporosity and
415 water flow patterns using computed tomography, *Soil Use and Management*, 18(2), pp. 142–151.
416 doi: 10.1079/SUM2002121

417 Mooney, S., Pridmore, T., Helliwell, J. & Bennett, M. (2012) Developing X-ray computed tomography
418 to non-invasively image 3-D root systems architecture in soil, *Plant and Soil*, 352, pp. 1–22.

419 Muddle, D.E. (2017). *The effects of soil macroporosity on the hydrology of infrastructure slopes*.
420 Thesis (Ph.D.) - University of Bath, 2017.

421 Munkholm, L.J., Heck, R.J. and Deen, B. (2012) 'Soil pore characteristics assessed from X-ray micro-
422 CT derived images and correlations to soil friability', *Geoderma*, 181–182, pp. 22–29. doi:
423 10.1016/j.geoderma.2012.02.024.

424 Naveed, M., Moldrup, P., Arthur, E., Wildenschild, D., Eden, M., Lamandé, M., Vogel, H.J. and De
425 Jonge, L.W. (2013). Revealing soil structure and functional macroporosity along a clay gradient using
426 X-ray computed tomography. *Soil Science Society of America Journal*, 77(2), pp.403-411.

427 O'Brien, A.S., Ellis, E.A. and Russell, D. (2004). Old railway embankment clay fill–laboratory
428 experiments, numerical modelling and field behaviour. In Advances in geotechnical engineering*: The
429 Skempton Conference.* Thomas Telford, London, pp. 911-921.

430 O'Brien, A.S. (2013). The assessment of old railway embankments – time for a change? *Partial
431 Saturation in Compacted Soils: Géotechnique Symposium in Print 2011*, pp. 19–32
432 (http://dx.doi.org/10.1680/geot.sip11.ks)

433 Ommaya, A.K., Murray, G., Ambrose, J., Richardson, A. and Hounsfield, G. (1976). Computerized axial
434 tomography: estimation of spatial and density resolution capability. *The British Journal of Radiology*,
435 49(583), pp.604-611.

436 Pender, M.J., Kikkawa, N. and Liu, P. (2009). Macro-void structure and permeability of Auckland
437 residual clay. *Geotechnique*, 59(9), pp.773-778.

438 Perret, J., Prasher, S.O., Kantzas, A. and Langford, C. (1999). Three-dimensional quantification of
439 macropore networks in undisturbed soil cores. *Soil Science Society of America Journal*, 63(6),
440 pp.1530-1543.

441   Peth, S., Nellesen, J., Fisher, G., Beckman, F. and Horn, R. (2010). Dynamics of soil pore space
442   structure investigated by X-ray microtomography. In *19th World Congress of Soil Science, Soil*
443   *Solutions for a Changing World, Brisbane, Australia*, pp.17-20.

444   Powrie, W. (2014). Soil mechanics: concepts and applications. *CRC Press*. London.

445   Rowe, P.W. (1972). The relevance of soil fabric to site investigation practice. *Geotechnique*, 22(2),
446   pp.195-300.

447   Scott, J.M., Loveridge, F. and O'Brien, A.S. (2007). Influence of climate and vegetation on railway
448   embankments. In: Cue'llar, V., Dapena, E., Alonso, E., *et al*. (Eds.), *Proceedings of the 14th European*
449   *Conference on Soil Mechanics and Geotechnical Engineering, Madrid*. Millpress, Amsterdam, the
450   Netherlands, pp. 659–664.

451   Schindelin, J., Arganda-Carreras, I., Frise, E., Kaynig, V., Longair, M., Pietzsch, T., Preibisch, S.,
452   Rueden, C., Saalfeld, S., Schmid, B. and Tinevez, J.Y.(2012) 'Fiji - an Open Source platform for
453   biological image analysis', *Nature methods*, 9(7), p. 10.1038/nmeth.2019. doi: 10.1038/nmeth.2019.

454   Shin, H. S., Kim, K. Y. and Pande, G. N. (2013) 'Porosity and Pore-Size Distribution of Geomaterials
455   from X-ray CT Scans', in Laloui, L. and Ferrari, A. (eds) *Multiphysical Testing of Soils and Shales SE -*
456   *21*. Springer Berlin Heidelberg (Springer Series in Geomechanics and Geoengineering), pp. 177–186.
457   doi: 10.1007/978-3-642-32492-5_21.

458   Smith, J. C. (2015) Examining Soil Based Construction Materials through X-Ray Computed
459   Tomography. Thesis (Ph.D.) Durham University.

460   Spearman, C. (1904). The proof and measurement of association between two things. *The American*
461   *Journal of Psychology*, 15(1), pp.72-101.

462   Taina, I.A., Heck, R.J. & Elliot, T.R. (2008) 'Application of X-ray computed tomography to soil science:
463   a literature review', *Canadian Journal of Soil Science*, 88, pp. 1–19.

464   Terzaghi, K. (1943). Theory of consolidation. *Theoretical Soil Mechanics*, pp.265-296.

465   Vaughan, P.R., Kovacevic, N., Potts, D.M. (2004). Then and now: some comments on the design and
466   analysis of slopes and embankments. Advances in Geotechnical Engineering. *The Skempton*
467   *Conference*. Thomas Telford, London, pp. 241–290.

468   Wildenschild, D. and Sheppard, A.P. (2013) 'X-ray imaging and analysis techniques for quantifying
469   pore-scale structure and processes in subsurface porous medium systems', *Advances in Water*
470   *Resources*. Elsevier Ltd, 51, pp. 217–246. doi: 10.1016/j.advwatres.2012.07.018.

471   Washburn, E.W. (1921).The dynamics of capillary flow. *Physical Review*, 17(3), p.374

472

7. Tables

Table 1: The labels and details of the samples excavated from Laverton Embankment (both in situ and saturated conditions shown)

Table 2: The XCT scanner settings used to scan samples from Laverton Embankment

Table 3: The voxel resolution achieved from XCT scan of the 100 mm diameter clay fill core samples from Laverton Embankment. The greyscale threshold values (256 levels) are shown in brackets.

Table 4: The pore property metrics for 40 mm cubed (central) sub volumes of clay fill calculated using XCT image data

Table 5: Mercury Intrusion Porosimetry (MiP) results and total porosity for Sample $5C_{(bot)}$ and the Reconstituted Sample.

Table 6: Porosity and saturated hydraulic conductivity measurements from triaxial permeability tests and one-dimensional consolidation tests on the saturated clay fill samples

8. Figures

Figure 1: Laverton Embankment in Gloucestershire as viewed (a) from the road, (b) from above.

Figure 2: A profile showing the volume of voids throughout the height of Sample 5C. This profile is composed of data from three individual sub volumes (40 mm sub volumes) at the top, the middle and the bottom of the sample

Figure 3: Three dimensional visualisations of macropore structure within 40 mm sub volumes of (a) Initial Sample 5C $_{(bot)}$,(b) Saturated Sample 5C$_{(bot)}$, (c) The Reconstituted Sample. These samples had a corrected macroporsity of 58%, 53% and 40% respectively (Table 4).

Figure 4: Profiles showing the volume of voids per slice for each of the samples, located between 1.5-6.5 m below the embankment surface.

Figure 5: Profiles showing the volume of voids within per slice (%) from the XCT data before and after sample saturation for samples (a) 2C, (b) 3C and (c) 4C.

Figure 6: Spearman's correlation coefficients for the pore property metrics from the saturated clay fills samples and the laboratory hydraulic conductivity measurements.

Figure 7: A flowchart outlining the key stages of the XCT image analysis procedure.

Figure 8: A midsection slice from the reconstituted sample image data (40 mm cube sub volume) subjected to (a) no filter, (b) a median filter, (C) a sharpened median filter, (d) a non-local means filter, and (e) a Gaussian filter.

Figure 9: Greyscale intensity histograms for the reconstituted sample after the application of image enhancement techniques (shown in images).

Figure 10: A midsection slice through the reconstituted sample (40 mm cube sub volume) (a) prior to segmentation, (b) after thresholding using the fully automated watershed method, (c) after manual thresholding using the interactive method. The pores are shown as black. The segmented pores are shown as blue.

Figure 11: The impact of partial volume correction (2 voxels) on pore volume throughout the reconstituted sample.

9. Appendix

An initial investigation was used to develop the image analysis procedure for the clay fill samples (Muddle, 2017) by first examining a reconstituted clay fill sample (100 mm diameter, 87 mm height). A flowchart outlining the key stages of the XCT image analysis procedure is shown in Figure 7. The details of the filtering, thresholding and partial volume correction stages are described below.

Figure 8 shows images of the midsection slice from a 40 mm sub volume of the reconstituted clay fill sample with different applied filters. All of the filters reduced the level of noise present within the images. The sharpened median filter and the non-local mean filter gave the sharpest contrast between phases with the most defined pore edges. The Gaussian filter and the median filter showed blurring of the pore boundaries. Examination of the greyscale intensity histograms (Figure 9) shows that the median and Gaussian filters did not significantly improve the definition of the material phase peaks within the greyscale histograms. The sharpened median filter and the non-local means filter improved the image quality and the definition of peaks. The sharpened median filter was twice as computationally efficient as the non-local means filter and was therefore selected for the subsequent analyses.

The effectiveness of automated watershed thresholding in relation to interactive manual thresholding was compared by visual assessment of slices throughout the height of the reconstituted clay fill sample. Figure 10a shows an image with a sharpened median filter prior to segmentation. This can be compared with the same slice after the application of automated watershed thresholding (Figure 10b) and the manual method (Figure 10c). These Figures show that the automated thresholding method produced more unsegmented pores than the manual method. The manual method was a more reliable segmentation method than the automated method for a sample of clay fill with intensity histograms lacking complete definition.

All objects with an equivalent diameter less than two voxels ($106\text{-}126 \times 10^{-6}$ m) were removed from the image data prior to quantification of the macropore property metrics. The partial volume correction removed a large number of objects from the images for the reconstituted sample. This is because the reconstituted sample had a relatively uniform pore size and distribution, with few large macropores compared to the number of smaller macropores. While a large number of pores were removed, particularly in the largest sub volume, the volume of removed pores was small. The effect of a two voxel partial effect correction on the total calculated macroporosity was between 0.02 % and 0.04 % of sample volume depending on the size of the subsample.

Figure 11 shows the influence of the partial volume correction on the profile of volume of pores per slice through the height of the reconstituted sample. The correction does not significantly alter the profile, with the exception of one section at the centre of the subsample with a higher macroporosity. The difference indicates that the increase in macroporosity in the middle slices was due to many individual, small macropores rather than fewer, larger macropores. The measured increase in macroporosity was a consequence of the laboratory preparation of the reconstituted sample.

7. Tables

Table 1: The labels and details of the samples excavated from Laverton Embankment (both in situ and saturated conditions shown)

	2C	2C saturated	3C	3C saturated	4C	4C saturated	5C-top	5C-top saturated	5C-mid	5C-bot	5C-bot saturated	6C	6C saturated	7C*	Reconstituted
Height ($\times 10^{-3}$ m)	98	86	87	80	92	78	92	83	107	94	75	91	78	92	87
Diameter ($\times 10^{-3}$ m)	102	102	102	102	102	102	102	102	102	102	102	87	87	87	100
Bulk density ($\times 10^{-3}$ kg/m³)	1.75	1.73	1.79	1.79	1.85	1.91	1.80	1.79	1.84	1.84	1.89	1.81	1.85	1.87	1.91
Origin - depth of centre of sample from the surface (m)	1.50	1.50	2.51	2.51	3.51	3.51	4.50	4.50	4.54	4.58	4.58	5.51	5.51	6.51	3.58
Water content (gravimetric %)	25	31	26	34	26	29	26	29	26	26	30	25	33	24	33

* Sample 7C could not be saturated and rescanned due to the fragmented nature of the sample

Table 2: The XCT scanner settings used to scan samples from Laverton Embankment

Sample	Voltage (kV)	Current (mA)	Exposure (ms)	Projections	Vertical slices	Other
102 or 87 mm diameter cylindrical sample	195	105	2000	1800	1998	Copper* filter (0.5 mm thick)

* Copper filter used to reduce beam hardening

Table 3: The voxel resolution achieved from XCT scan of the 100mm diameter clay fill core samples from Laverton Embankment. The greyscale threshold values (256 levels) are shown in brackets.

Sample	Voxel resolution ($\times 10^{-6}$ m)	Sample	Voxel resolution ($\times 10^{-6}$ m)	Sample	Voxel resolution ($\times 10^{-6}$ m)
2C (25)	58.2	5C-top*[2] (50)	57.3	6C (48)	53.4
2C saturated*[1] (26)	61.1	5C-top saturated*[1] (53)	61.5	6C saturated*[1] (53)	52.9
3C (48)	54.8	5C-mid*[2] (55)	53.7	7C (60)	54.4
3C saturated*[1] (24)	60.4	5C-bot*[2] (46)	54.7	Recon (105)	62.7
4C (50)	55.5	5C-bot saturated*[1] (49)	59.7		
4C saturated*[1] (58)	58.2				

*[1] Saturated and unsaturated sample resolutions were matched using the PVE correction to allow for comparison between the samples.

*[2] The resolution of the three samples within 5C were matched using the PVE correction to allow for porosity throughout the height of the sample to be compared.

Table 4: The pore property metrics for 40 mm cubed (central) sub volumes of clay fill calculated using XCT image data

	2C	2C saturated	3C	3C saturated	4C	4C saturated	5C-top	5C-top saturated	5C-mid	5C-bot	5C-bot saturated	6C	6C saturated	7C	Reconstituted
Corrected Macroporosity (%)	1.98	0.81	2.03	1.72	0.38	0.15	1.85	1.80	1.30	0.58	0.53	0.18	0.11	4.12	0.40
Macropore density ($\times 10^6$) (number/m^3)	66.14	57.76	60.86	35.08	89.62	13.20	142.42	83.45	149.95	74.87	56.45	29.11	25.75	59.84	51.70
Mean macro pore length ($\times 10^{-3}$ m)	1.09	0.98	1.13	0.96	1.05	1.19	1.59	1.43	1.58	1.57	1.41	0.80	0.81	2.02	0.98
Surface area density (m^2/m^3)	207.87	110.62	198.45	188.52	86.00	19.76	264.18	209.68	203.25	88.81	70.68	34.75	23.76	337.64	69.15
Mean volume of ten largest pores ($\times 10^{-9}$ m^3)	55.28	13.93	70.57	72.90	6.82	4.47	36.69	21.19	16.16	8.53	6.51	5.68	2.41	203.44	4.42

Table 5: Mercury Intrusion Porosimetry (MiP) results and total porosity for Sample 5C$_{(bot)}$ and the Reconstituted Sample.

	5C-bot sample	Reconstituted sample
Mass of sample ($\times 10^{-3}$ kg)	0.49	1.39
Density ($\times 10^3$ kg/m^3)	1.78	1.91
Volume of sample ($\times 10^{-9}$ m^3)	275.83	730.05
Total specific volume of pores ($\times 10^{-6}$ m^3/kg)	152.34	134.73
Total pore volume ($\times 10^{-9}$ m^3)	74.62	187.72
Max pore entrance diameter ($\times 10^{-6}$ m)	109.52	110.01
Min pore entrance diameter ($\times 10^{-6}$ m)	0.0037	0.0037
Average pore entrance diameter ($\times 10^{-6}$ m)	0.023	0.024
Modal pore entrance diameter ($\times 10^{-6}$ m)	0.051	0.052
Median pore entrance diameter ($\times 10^{-6}$ m)	0.042	0.043
MIP Porosity (%)	27	26
Total porosity (phase relationship) (%)	45	50

Table 6: Porosity and saturated hydraulic conductivity measurements from triaxial permeability tests and one-dimensional consolidation tests on the saturated clay fill samples

	2C saturated	3C saturated	4C saturated	5C-top saturated	5C-bot saturated	6C saturated	Reconstituted sample
Total porosity (%)	50	49	44	48	45	48	50
Oedometer (3 x 70 mm diameter, 20 mm height) - average saturated hydraulic conductivity (first loading step) ($\times10^{-10}$ m/s)	17.7	6.24	7.35	3.75	16.5	2.26	2.95
Triaxial (100 mm diameter, 80 mm height) - saturated hydraulic conductivity ($\times10^{-11}$ m/s)	10.4	5.32	16.7	80.3	10.8	1.76	8.15
Factor of difference between oedometer and triaxial measured saturated hydraulic conductivity	17.0	11.7	4.4	4.7	15.3	12.8	3.6

8. Figures

(a)

(b)

Figure 1: Laverton Embankment in Gloucestershire as viewed (a) from the road, (b) from above.
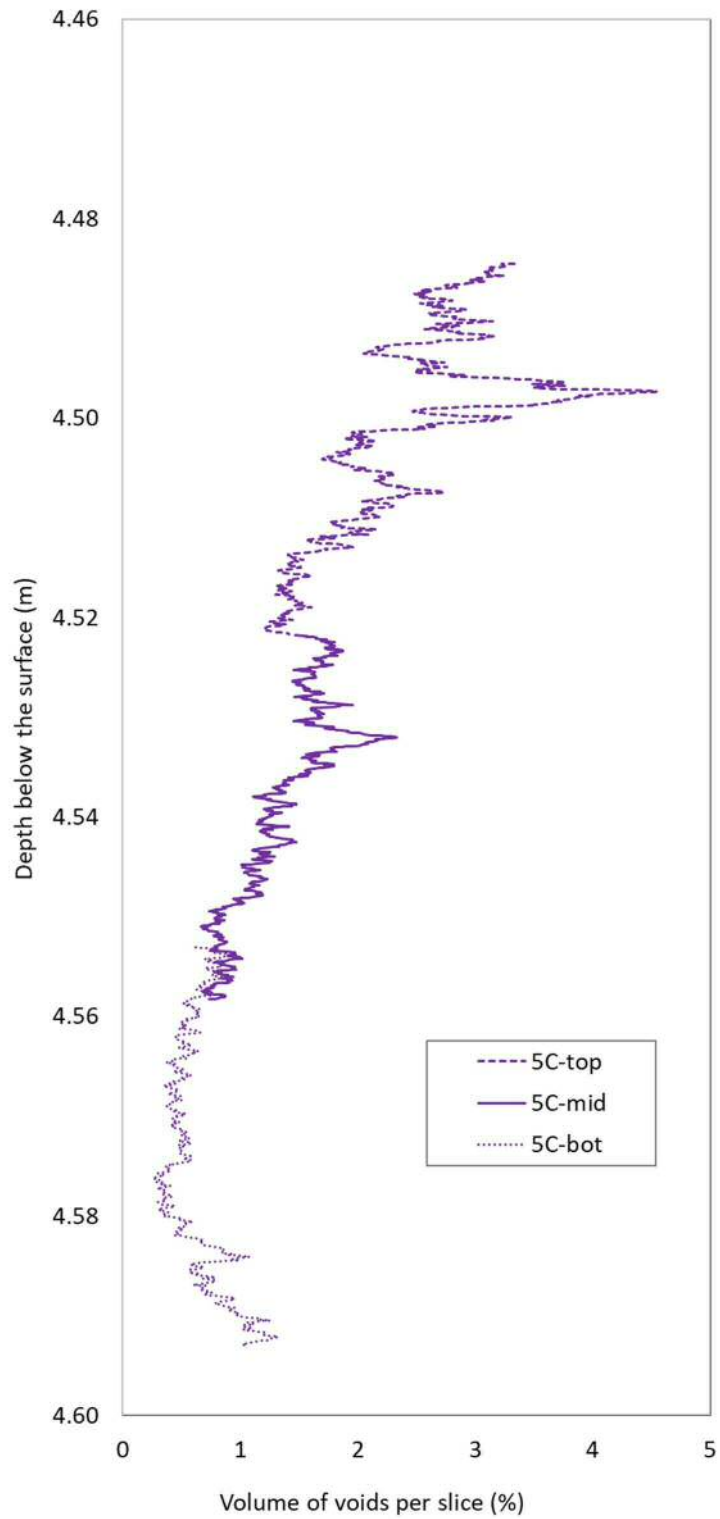
Figure 2: A profile showing the volume of voids throughout the height of Sample 5C. This profile is composed of data from three individual sub volumes (40 mm sub volumes) at the top, the middle and the bottom of the sample.
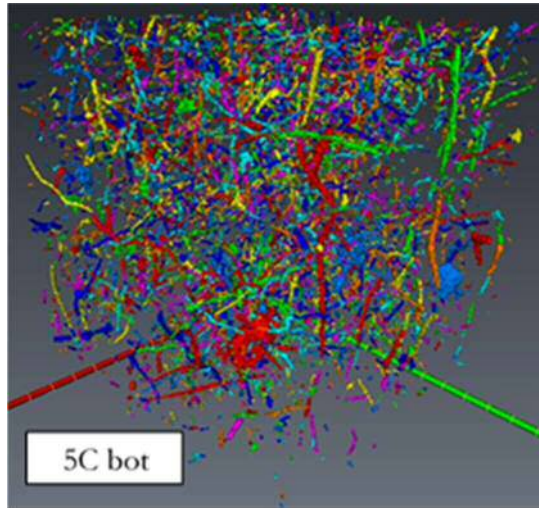
(a)
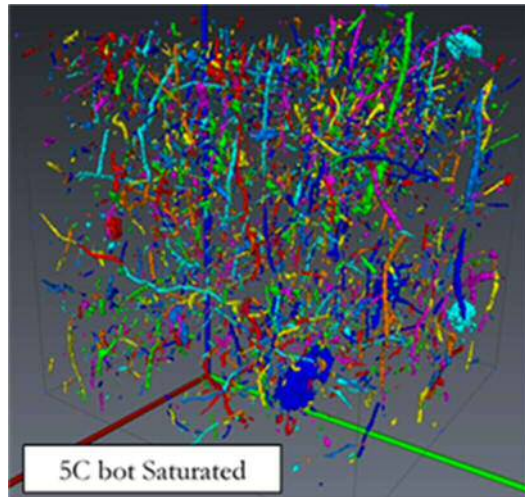
(b)
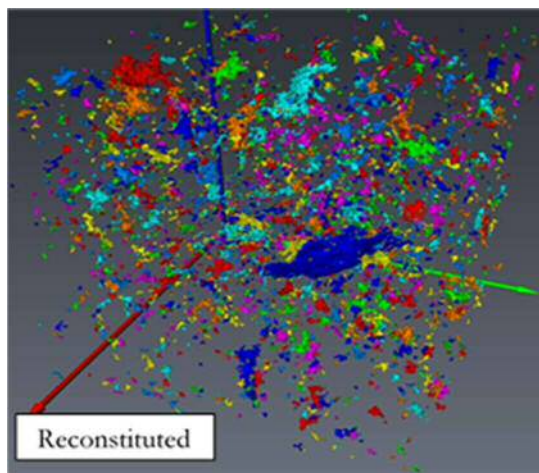
(c)

Figure 3: Three dimensional visualisations of macropore structure within 40 mm sub volumes of (a) Initial Sample 5C (bot) ,(b) Saturated Sample 5C(bot), (c) The Reconstituted Sample. These samples had a corrected macroporsity of 58%, 53% and 40% respectively (Table 4).
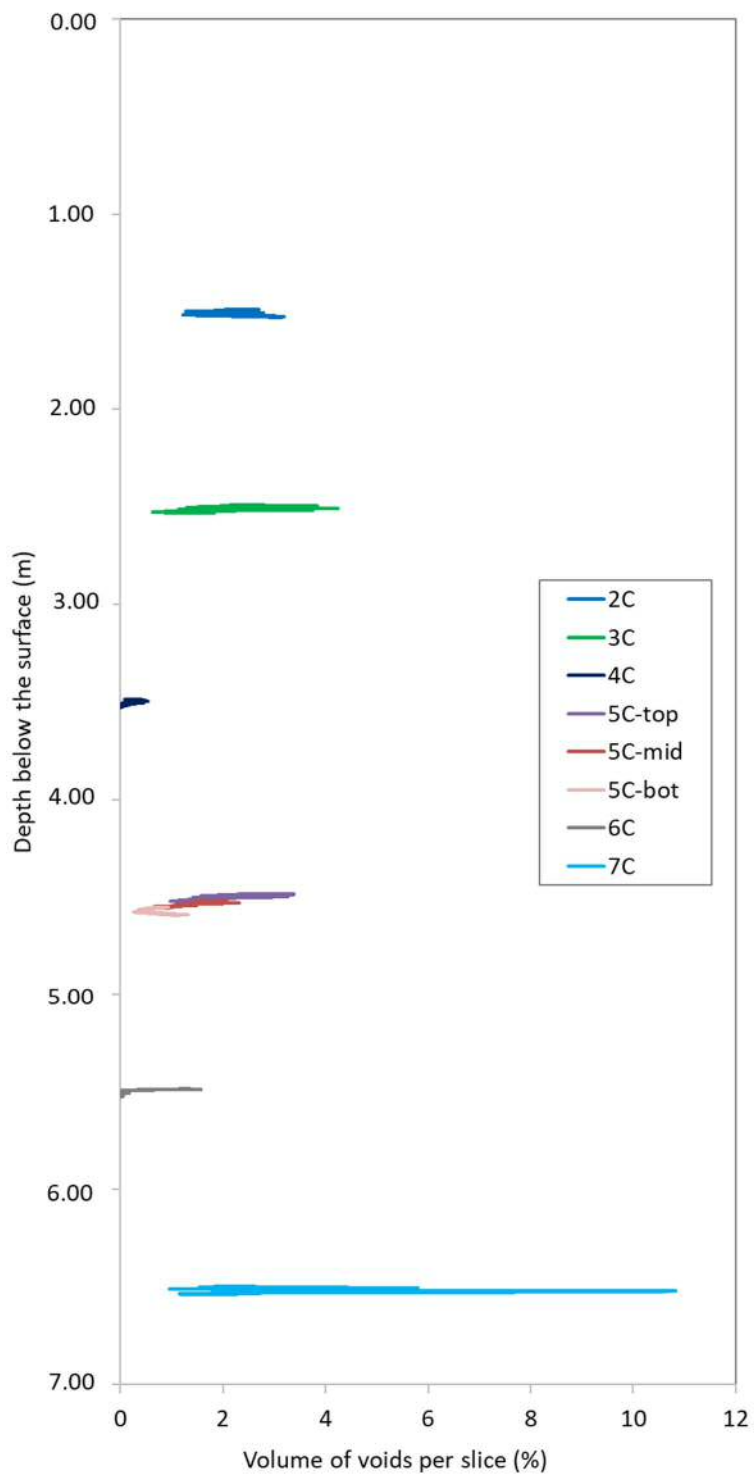
Figure 4: Profiles showing the volume of voids per slice for each of the samples, located between 1.5-6.5m depth below the embankment surface.
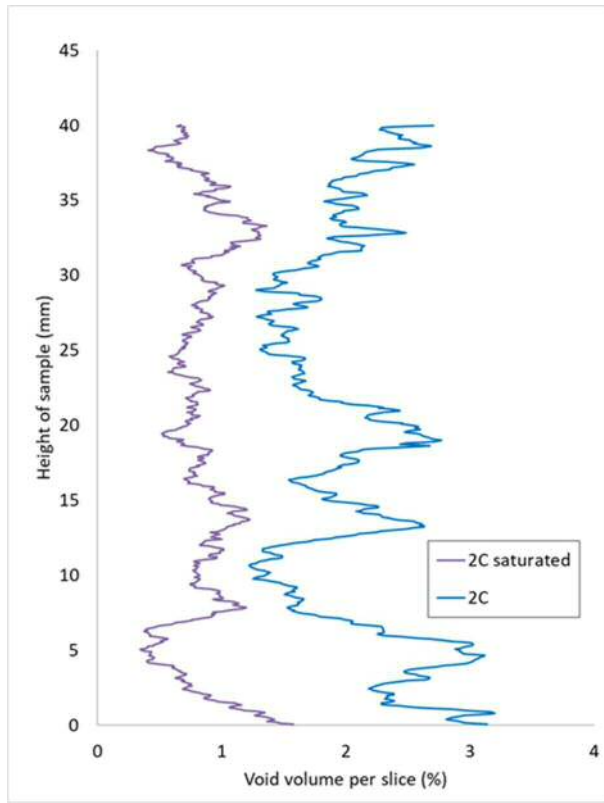
(a)
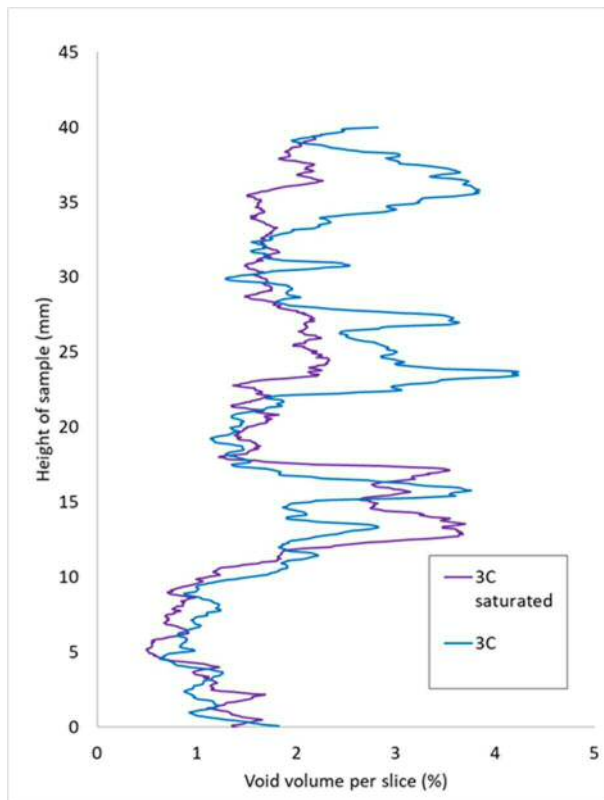
(b)
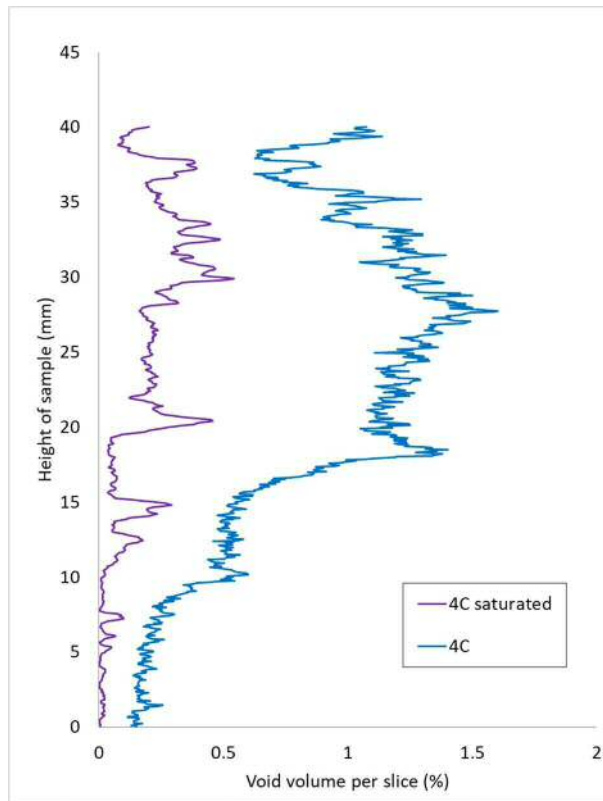
(c)

Figure 5: Profiles showing the volume of voids within per slice (%) from the XCT data before and after sample saturation for samples (a) 2C, (b) 3C and (c) 4C.

Spearman's Rho coefficients	Triaxial saturated hydraulic conductivity	Oedometer saturated hydraulic conductivity	Total porosity (phase relationship)	Bulk density	Corrected XCT-derived macroporosity	Macropore density	Mean macropore length	Macropore surface area density	Mean volume of ten largest XCT-observed macropores
Triaxial saturated hydraulic conductivity									
Oedometer saturated hydraulic conductivity	0.82								
Total porosity (phase relationship)	-0.45	-0.11							
Bulk density	0.07	-0.47	-0.43						
Corrected XCT-derived macroporosity	0.39	0.71	0.29	-0.65					
Macropore density	0.43	0.75	0.38	-0.56	0.75				
Mean macropore length	0.96	0.86	-0.42	0.02	0.46	0.57			
Macropore surface area density	0.21	0.61	0.38	-0.75	0.96	0.79	0.32		
Mean volume of ten largest XCT-observed macropores	0.32	0.64	0.15	-0.65	0.93	0.5	0.36	0.86	

Legend:
- 0.8 to 1
- 0.6 to 0.8
- 0.4 to 0.6
- 0.2 to 0.4
- 0.0 to 0.2
- 0.0
- 0.0 to -0.2
- -0.4 to -0.6
- -0.6 to -0.8
- -0.8 to -1

Figure 6: Spearman's correlation coefficients for the pore property metrics from the saturated clay fills samples and the laboratory hydraulic conductivity measurements.

Image acquisition and reconstruction: Using Nikon X-Trek XTH225ST . Data were reconstructed using the Nikon proprietary filtered back projection algorithm, with a voxel resolution of 53-62 μm

↓

Extraction of a 40mm cubed subsample: From the centre of the sample.

↓

Image filtering: Using a sharpened median filter to smooth data, reduce noise and remove artefacts.

↓

Image sharpening: To define the material phases

↓

Thresholding and segmentation: Using interactive manual thresholding and segmentation

↓

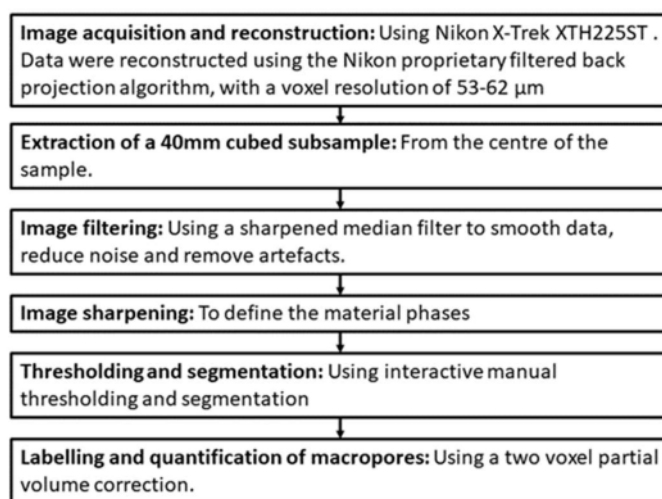**Labelling and quantification of macropores:** Using a two voxel partial volume correction.
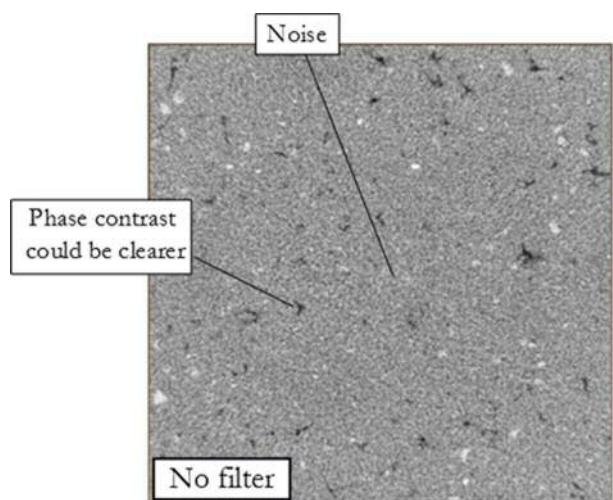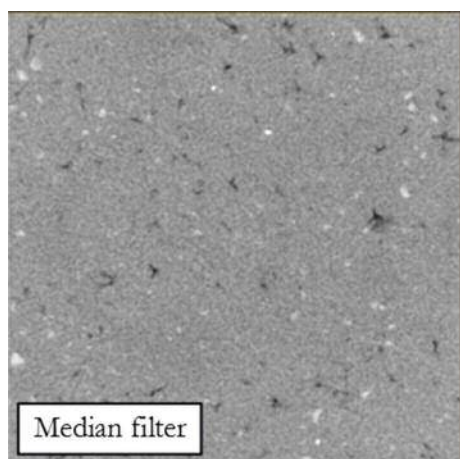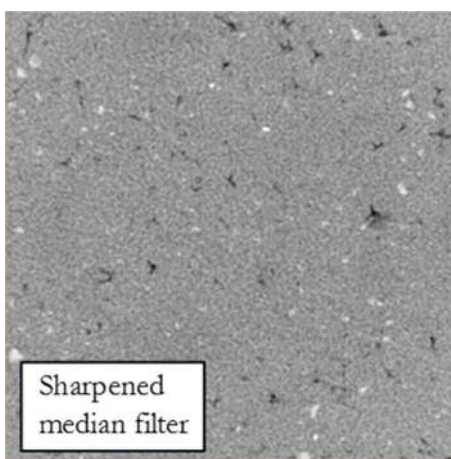
Figure 7: A flowchart outlining the key stages of the XCT image analysis procedure
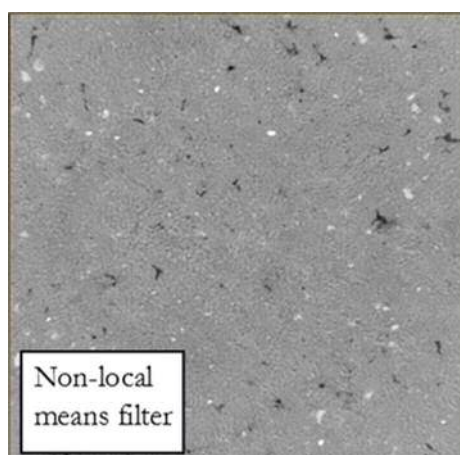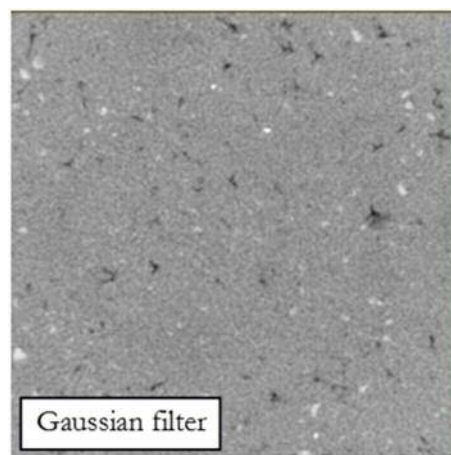
Figure 8: A midsection slice from the reconstituted sample image data (40 mm cube sub volume) subjected to (a) no filter, (b) a median filter, (C) a sharpened median filter, (d) a non-local means filter, and (e) a Gaussian filter.
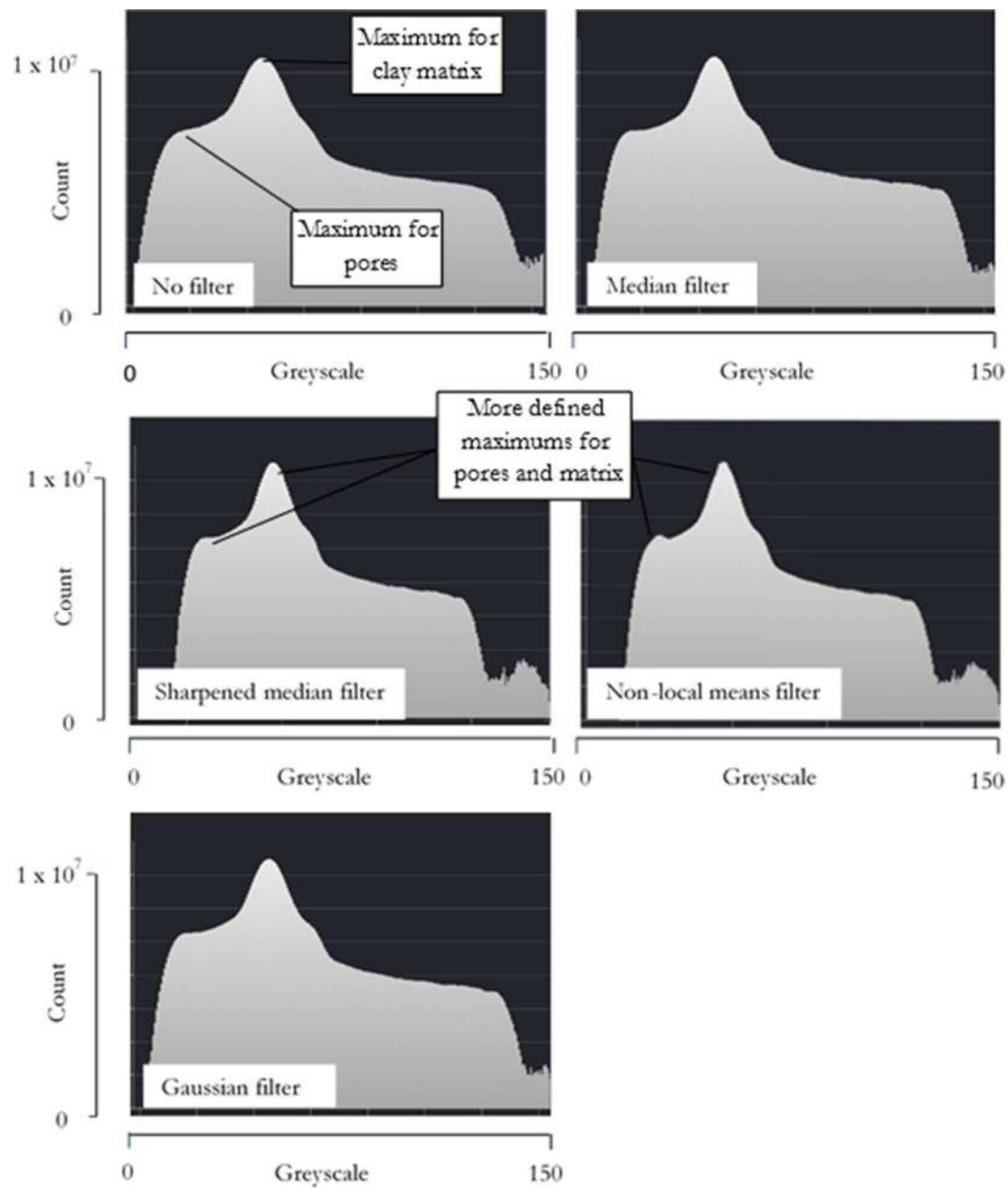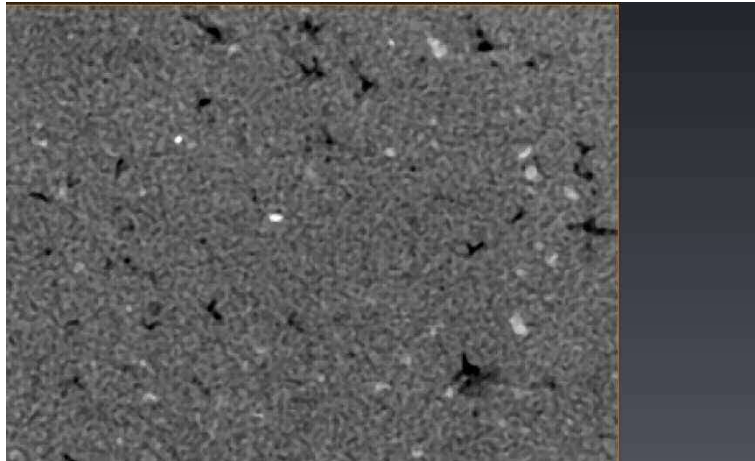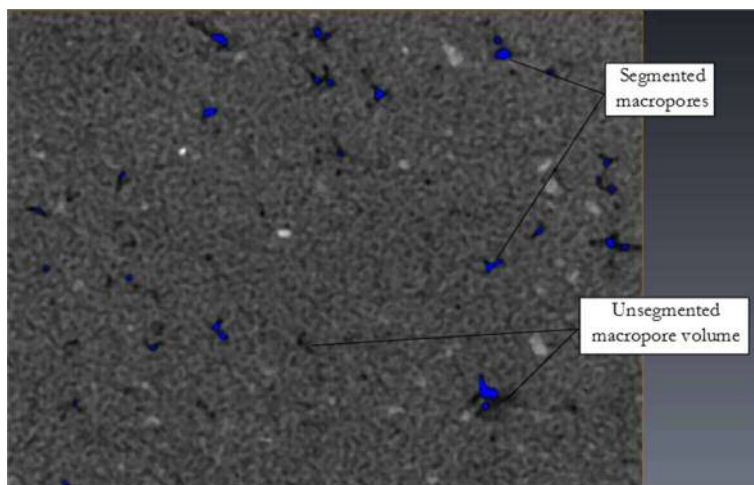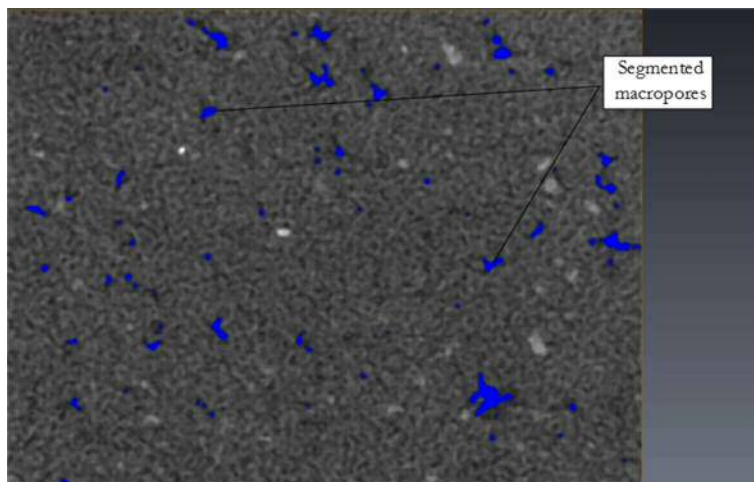
Figure 9: Greyscale intensity histograms for the reconstituted sample after the application of image enhancement techniques (shown in images).

(a)

(b)

(c)

Figure 10: A midsection slice through the reconstituted sample (40 mm cube sub volume) (a) prior to segmentation, (b) after thresholding using the fully automated watershed method, (c) after manual thresholding using the interactive method. The pores are shown as black. The segmented pores are shown as blue.
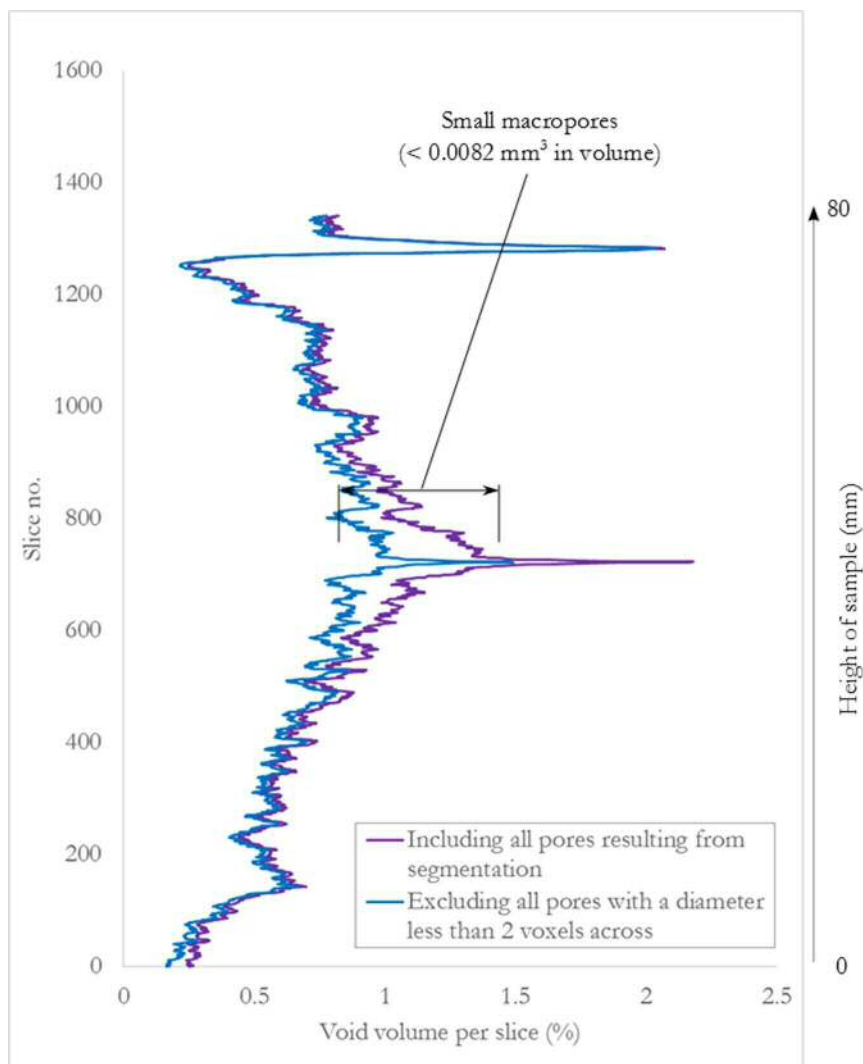
Figure 11: The impact of partial volume correction (2 voxels) on pore volume throughout the reconstituted sample.